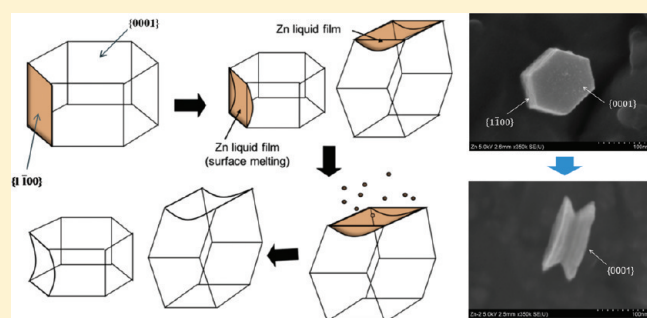


# Evaporation Anisotropy of Free Nanocrystals

Xiaofei Ma, Anshuman A. Lall, George W. Mulholland, and Michael R. Zachariah\*

Department of Mechanical Engineering and Department of Chemistry and Biochemistry, University of Maryland-College Park, College Park, Maryland 20742, United States

**ABSTRACT:** We report observations of the evaporation anisotropy of substrate-free Zn nanocrystals (NCs) as imaged from electron microscopy and determine the onset temperature of evaporation as a function of NC size by the gas-phase ion-mobility method. The observed shape transformation of free NCs is fundamentally different from those observed in traditional hot-stage TEM heating experiments. The onset temperature for evaporation decreases as the NC size decreases and is analogous to the Kelvin effect. The cohesive energy of bulk Zn is determined to be  $1.8 \pm 0.1$  eV from the size-dependent evaporation data. A mechanism based on crystal face dependent surface melting is proposed to explain the evaporation anisotropy effect.



## INTRODUCTION

Phase transitions of nanocrystal/nanoparticles are of interest because of their size-dependent properties. Examples include melting point depression<sup>1–3</sup> (one of the oldest areas of small particle research) and size-dependent evaporation.<sup>4,5</sup> Furthermore, morphology changes are often accompanied by phase transitions.<sup>6–8</sup>

The prospect of exploiting these properties to create new functional materials and advanced devices has become the primary motivation for this multidisciplinary research area. For example, in the area of catalysis, accurate measurement of the transition temperature as a function of particle size helps determine the thermal stability regime of different sizes of catalytic particles, whereas the ability to control the shape of NCs can change their catalytic ability.<sup>9,10</sup>

As the crystal becomes smaller, there is a higher proportion of atoms on the surface with fewer nearest neighbors and are thus more weakly bound and less constrained in their thermal motion than the bulk. Furthermore, atoms on different types of crystal faces have different bonding, surface atom densities, and electronic structure, and thus, their properties are expected to be different. Previous experiments have shown that the physical processes, such as surface diffusivity<sup>11</sup> and surface melting, are crystal face dependent,<sup>12</sup> and the chemical reaction rates are anisotropic.<sup>13–15</sup> Central to many anisotropic effects in crystals is the anisotropy of the surface free energy. The surface energy defined as the energy required to create a unit area of new surface plays an essential role in nanocrystal/nanoparticle processes such as melting, coalescence, and evaporation; it also determines the equilibrium shape, faceting, and growth of NCs. For example, the equilibrium shape of small particles can be achieved under prolonged heating at elevated temperatures by minimization of the total surface free energy. According to a Wulff construction,

the equilibrium crystal shape is related to the polar plot of the specific surface energy. Chemical reactivity can also be affected by the surface energy anisotropy. As pointed out by Madey,<sup>16</sup> the anisotropy in surface free energy can be enhanced considerably when the surface is covered by gaseous or metallic impurities. This enhanced surface energy anisotropy will facilitate the faceting on crystal surfaces which could greatly alter the reactivity of surfaces. The ability to control the surface reactivity is of major importance to modern catalytic applications.

Zn is an important component in many applications. It is the fuel in the zinc-air fuel cell, and an anode material in batteries. More recently, Zn/ZnO redox reactions have been considered for thermochemical two-step water-splitting cycles for hydrogen generation.<sup>17</sup> The cycle involves a Zn hydrolysis reaction to produce hydrogen, followed by the solar reduction of zinc oxide. The crystal structure of zinc is hexagonal close-packed (hcp), which belongs to the space group  $P63/mmc$ . For hcp metals, the basal plane (0001) is the most close-packed and also has the minimum surface energy.<sup>18</sup> The variation in surface energies of different crystal planes is expected to lead to the difference in thermal stability and thus a difference in anisotropy effects during phase transitions.

In this study, in situ generated free (unsupported) Zn NCs were chosen as the platform to study the anisotropy in evaporation. Free NCs are suspended in an inert gas environment, i.e. substrate free; and thus, all crystal planes are coexistent and exposed to the same experimental conditions simultaneously. We used an online tandem gas-phase ion-mobility method, together with off-line electron microscopy to characterize the Zn NCs.

Received: June 30, 2011

Revised: July 18, 2011

Published: July 25, 2011

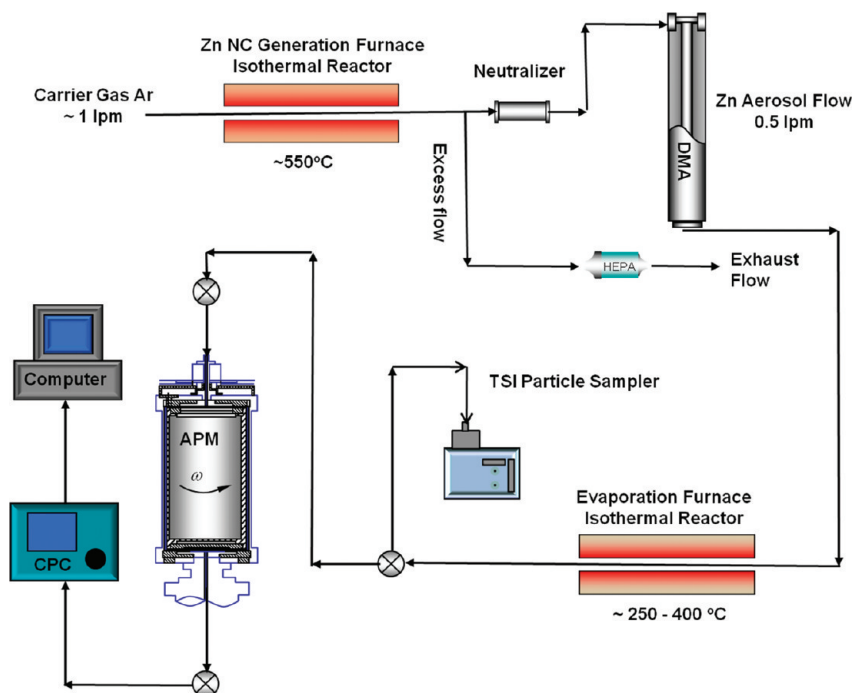


Figure 1. Schematic of the experiment system.

The size-dependent evaporation temperature is determined by ion-mobility measurements, whereas the NC shape transformation is observed by electron microscopic analysis.

## EXPERIMENTAL METHODS

A schematic of the experimental setup is presented in Figure 1. The details of the DMA-APM experimental system have been previously described.<sup>13,19</sup> In brief, the experimental system consists of four parts: (a) generation of Zn NCs by evaporation–condensation, (b) size selection to generate monodispersed Zn NC in the aerosol phase using a differential mobility analyzer (DMA),<sup>20–22</sup> (c) heating of Zn NCs in a temperature-controlled tube furnace, and (d) measurement of the mass change resulting from evaporation using an aerosol particle mass analyzer (APM).<sup>23</sup> Previous studies<sup>4,5</sup> have studied evaporation from aerosols using a tandem DMA technique to monitor the size change of spherical particles. However, the interpretation of ion-mobility data is based on an assumption that the particles are spherical and can lead to considerable errors, particularly for the case investigated in this study. In this study, we combine the DMA with an APM which gives a direct measure of particle mass regardless of shape. Our DMA-APM mass measurements of NIST SRM 60 and 100 PSL spheres were within about 1.4% and 5.6%, respectively.<sup>24</sup> We have employed the DMA-APM technique previously to study the oxidation kinetics of nickel nanoparticles<sup>25</sup> and Zn NCs.<sup>13</sup>

Zn NCs are generated by evaporating granular Zn (purity,  $\geq 99.99\%$ , Sigma-Aldrich) at 550 °C with a tube furnace in a carrier gas of argon at 1 LPM (liter per minute). Unagglomerated single crystal Zn NCs are formed at the exit of the flow tube by empirical adjustment of the furnace temperature and the argon carrier gas flow rate. In our experiment, Zn NCs of ion-mobility sizes of 50 nm, 70 nm, 100 nm, and 150 nm were selected using the DMA as a band-pass filter in sequential experiments to study the size-dependent evaporation. After size classification,

the aerosol is passed through a second tube furnace, which allows controlled evaporation of the size selected NCs. The residence time of the aerosol in this furnace is about 5 s (30 cm length) at an argon flow of 0.5 LPM. The changes in NC masses are monitored by the APM downstream. The temperature in the evaporation furnace was set between 250–400 °C in increments of 25 °C. The particle mass distribution was then measured for each furnace temperature after the system reached its steady state. The room temperature particle mass distribution was also taken and was set as the base of the mass measurements. Samples for electron microscopy analysis were collected downstream from the evaporation furnace by electrostatically precipitating the aerosol onto a TEM grid.

## RESULTS AND DISCUSSION

Figure 2a shows SEM images of a single 100 nm Zn NC, which exhibits a perfect hexagonal prism shape. EDS (energy dispersive X-ray spectroscopy) spectra obtained from the NCs in the SEM confirmed the composition as Zn. Selected area electron diffraction analysis indicated that the Zn NCs have top surfaces of {0001} and side surfaces of {1 $\bar{1}$ 00} crystal planes.

**Morphological Evolution.** Figure 2b,c shows SEM and TEM images of a partially evaporated 100 nm mobility sized Zn NC collected after controlled evaporation at 375 °C for  $\sim 5$  s. As we can see from the images, most of the hexagonal-shaped top surfaces (Zn {0001} planes) of the Zn NCs are well-preserved relative to the side surfaces (Zn {1 $\bar{1}$ 00} planes) during evaporation. Material from the side surfaces and edges are preferentially etched away, which leaves the side surfaces with a depression while the top surfaces remain planar. Measurements also show that the widths of the side surfaces do not change. The reader is reminded that the evaporation takes place in the gas phase prior to deposition of the NC on the TEM grid.

To explain the observed evaporation anisotropy, we propose an evaporation mechanism based on the theory of surface

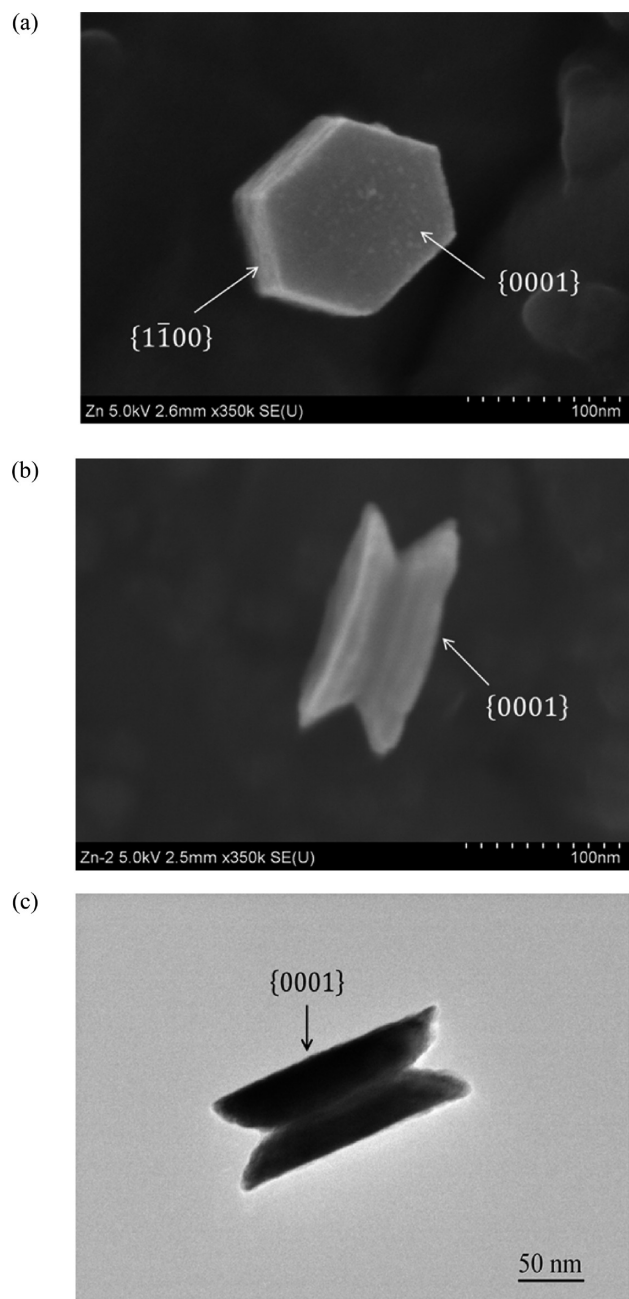


**Figure 2.** Images of aerosol grown hexagonal-prism-shaped Zn NCs: (a) SEM image of a Zn NC before evaporation, (b) SEM image of a partially evaporated Zn NC, and (c) TEM image of partially evaporated Zn NC.

melting. As Zn NCs enter the furnace region, the NCs are heated to the furnace temperature, which leads to premelting of some of the NC surfaces and edges; premelting describes the fact that, even below its melting point, quasi-liquid films can be observed on crystalline surfaces.<sup>26</sup> A thin layer of Zn quasi-liquid, an intermediate between those of the solid and the bulk liquid,<sup>26</sup> forms preferentially on the side surfaces ( $\{1\bar{1}00\}$  planes) of Zn NCs and on edges rather than on the more close-packed top surfaces ( $\{0001\}$  planes) due to the crystal-face-dependent surface melting.<sup>12</sup> At 375 °C, the energetic criterion of surface melting is met for Zn  $\{1\bar{1}00\}$  planes but not for Zn  $\{0001\}$

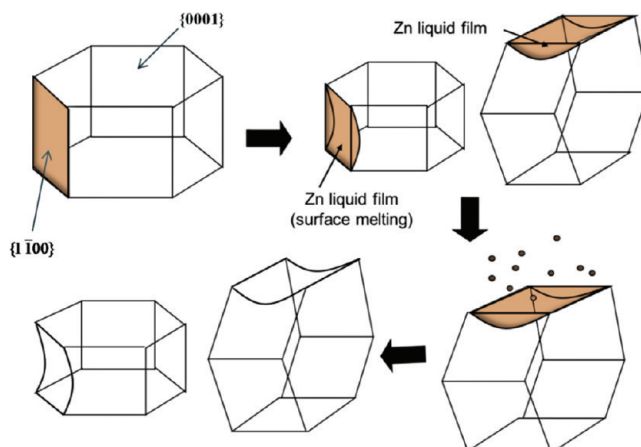


**Figure 3.** Evaporation mechanism of free Zn NC.

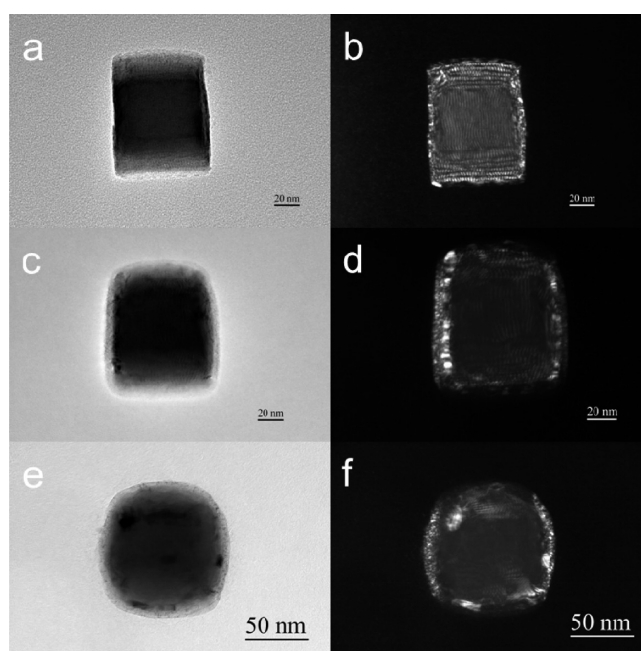


**Figure 4.** (a and b) Bright and dark field images of a side surface deposited NC before heating; (c and d) bright and dark field images taken after heating the NC at 300°C for ~5 minutes; (e and f) bright and dark field images taken after heating the NC at 325°C for ~6 minutes, the NC transforms into a spherical shape.

planes. The quasi-liquid layer over the side surfaces greatly enhances the evaporation rate so that a depression is formed. A schematic of the Zn NC evaporation mechanism is presented in Figure 3. This surface melting behavior is also believed to result in the enhanced evaporation of gold relative to that of silver nanoparticles.<sup>28</sup> We have observed an analogous anisotropy effect during the oxidation of free Zn NCs.<sup>13</sup> In both evaporation and oxidation, it is the  $\{1\bar{1}00\}$  plane that reacts preferentially. Furthermore, the reactivity and the evaporation rate are not homogeneous across the face, but are most active away from the interface with the  $\{0001\}$  surface. The behavior is consistent with the interface of the  $\{0001\}$  surface acting as a pinning site. This crystal-face-dependent melting and evaporation phenomena have a profound effect on ZnO nanowire growth. Both Law<sup>29</sup>

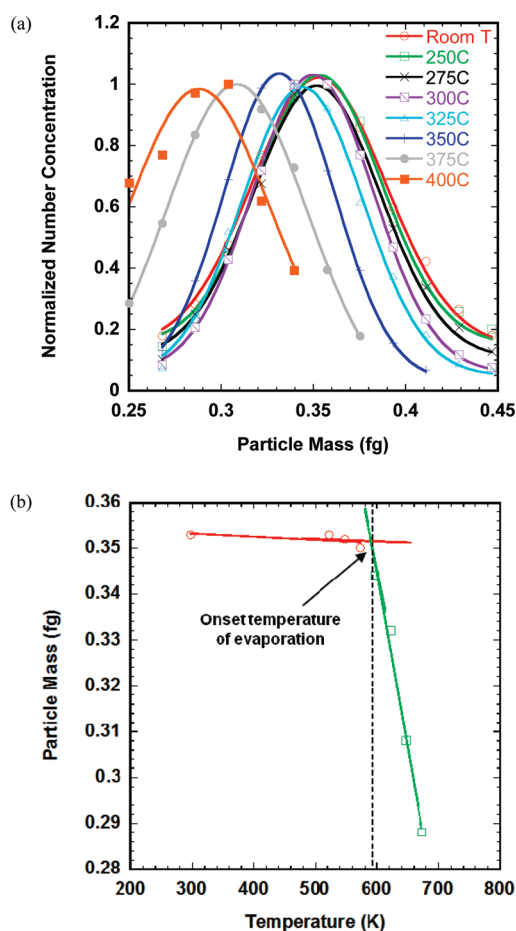


**Figure 5.** (a) Normalized particle mass distributions for the initial mobility NC size of 50 nm at different evaporation temperatures. (b) Particle mass vs temperature for the initial NC size of 50 nm. The intersection of two straight lines is the onset temperature of evaporation.

and Gao<sup>30</sup> found ZnO nanowires preferentially grow on the higher surface energy Zn  $\{1\bar{1}00\}$  surfaces. The mobile Zn atoms on the molten Zn surfaces thus readily react with free oxygen and form the oxide wire.

To compare the effect of different time–temperature heating histories on the morphology of NCs, an in situ TEM heating experiment was also conducted on Zn NCs (JEOL JEM 2100 LaB<sub>6</sub>). The sample was heated from room temperature up to 325 °C over a period of  $\sim 2$  min. Figure 4 shows bright and dark field TEM images of the  $\{1\bar{1}00\}$  plane, before and after heating. The fringe spacing in the dark field image for the before heating case is consistent with a hexagonal prism shape. After heating at 300 °C for  $\sim 5$  min, both the edges of the NC and the fringes in dark field image blur. After heating in the TEM at 325 °C for about 6 min, the  $\{1\bar{1}00\}$  plane transforms from a rectangular to a spherical shape, and the dark field indicates a lack of an ordered structure. The similar shape transformation has also been observed by Wang<sup>7</sup> for platinum NCs where he attributes the NC shape transformation to the surface premelting. To protect the TEM vacuum column, we were unable to go to higher temperatures for these Zn studies. However, isotropic evaporation from the surfaces of the spherical NC would be expected if we were to increase the temperature beyond 325 °C.

Clearly there are very significant differences between the shape changes observed between heating on a substrate and that of a

**Table 1.** Size-Dependent Evaporation Data for Different Sizes of Particles

temperature (K)	particle mass (fg)			
	50 nm	70 nm	100 nm	150 nm
298	0.353	0.973	2.91	8.4
523	0.353	0.971	2.91	8.4
548	0.352	0.970	2.91	8.4
573	0.350	0.970	2.90	8.4
598	0.344	0.970	2.91	8.3
623	0.335	0.953	2.89	8.1
648	0.312	0.917	2.65	7.8
673	0.288	0.811	2.26	7.4

free-NC. Unfortunately, because of instrumental constraints, the experimental conditions between the two heating conditions could not be matched. For the substrate heating case, since this was done within the TEM, we operated at a lower temperature for several minutes of heating. In contrast, the free NCs were heated to a higher temperature but for only  $\sim 1$  s. One might have expected that the higher temperature heating case (free NCs) would result in the more spherical shape, but in fact, the opposite is observed. One likely explanation is that the evaporation from the high energy plane is fast relative to surface diffusion, resulting in the observed anisotropy. However, in the substrate heating studies, the much longer heating period results in sufficient time for the molten or near molten surface to smear out the anisotropy.

The evolution in the morphology observed in Figure 2 suggests that fast evaporation and rapid quenching could be feasible techniques to produce particles with unique shapes by trapping them in metastable configurations.

**Size-Dependent Evaporation.** To study the size-dependent evaporation behavior of Zn NCs, we size select particles (with a DMA) and measure the resulting mass change (with an APM) after evaporation at different temperatures. A typical plot of normalized mass distributions of 50 nm mobility sized Zn NCs at different evaporation temperatures is shown in Figure 5a. At low temperatures, the particle mass distributions overlap with each other, i.e., evaporation is not occurring. Further increases in the furnace temperature results in a steady decrease in the mass distribution (i.e., mean particle mass). For each temperature, the peak mass of the NC mass distribution is calculated by fitting the experimental data using a Gaussian distribution and serves as the nominal mass of the monodispersed Zn NC population. The size-dependent evaporation data for other particle sizes is shown in Table 1. The accuracy in the mass measurement is a function of particle mass for the APM. For 50 nm and 70 nm particles, we have determined the accuracy to within 2%, while for 100 nm and 150 nm particles, the accuracy is determined to be  $\sim 5\%$ .<sup>24,31</sup> Figure 5b shows the measured NC mass vs temperature for 50 nm particles. The plot shows two regions, which can be represented by the best linear fits to the data. The near horizontal line represents the unevaporated case in which the mass of the NCs does not change, while the steeply sloped straight line represents an evaporation case. The onset temperature for evaporation for each mobility size is determined by finding the intersection of the two straight lines. From the experiment, even for the largest size of NCs (150 nm), the onset temperature of evaporation is lower than the bulk melting

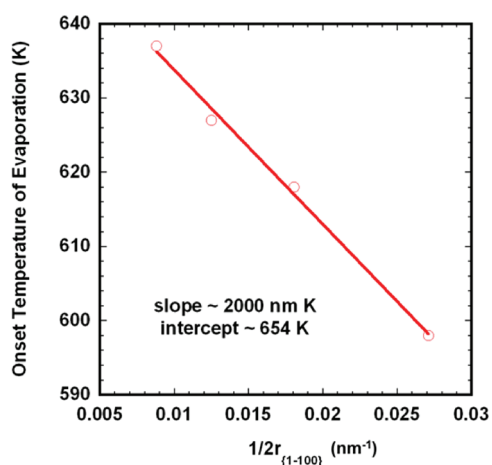


Figure 6. Onset temperature of evaporation vs  $1/2r_{\{1\bar{1}00\}}$ .

temperature of Zn (692 K). This result is consistent with the expected size dependence to colligative properties (e.g., evaporation temperature, melting point, etc.<sup>4,5</sup>).

Since the material evaporates, under the conditions studied here, almost exclusively from the  $\{1\bar{1}00\}$  plane, we define a characteristic radius,  $r$  as the distance from the center of the NC normal to the  $\{1\bar{1}00\}$  plane. On the basis of the room temperature mass measurement and the geometry of the synthesized NC, we obtain the characteristic diameter of our Zn NCs to be 39.6, 55.4, 80.0, and 113.6 nm corresponding to NCs of initial mobility diameters 50, 70, 100, and 150 nm, respectively. The onset temperature of evaporation is plotted against the inverse of the characteristic diameter of the NC as shown in Figure 6. A linear relationship gives a best fit with a slope of  $-2000 \pm 80 \text{ nm} \cdot \text{K}$  and an intercept of  $654 \pm 3 \text{ K}$ . The latter represents the temperature at which very large particles begin to evaporate, which compares to the reported bulk melting point of 692 K.

On the basis of previous studies,<sup>32–34</sup> the evaporation temperature can be scaled with the size-dependent atomic cohesive energy as follows:

$$\frac{T_{ev}(D)}{T_{ev}(\infty)} = \frac{E_B(D)}{E_B(\infty)} \quad (1)$$

where  $T_{ev}(D)$  is the evaporation temperature for particles of size  $D$ , while  $T_{ev}(\infty)$  represents the bulk evaporation temperature. Wang<sup>33</sup> simplified the functional form of  $(E_B(D))/E_B(\infty)$  and obtained a size-dependence evaporation temperature relationship similar to that of the size-dependence of the melting temperature:

$$T_{ev}(D) = T_{ev}(\infty) - \frac{hE_B(\infty)}{3RD} \quad (2)$$

where  $h$  is the atomic diameter, and  $R$  is the gas constant. Using our experimental slope of  $-2000 \text{ nm} \cdot \text{K}$  and  $h = 0.29 \text{ nm}$ <sup>35</sup> for Zn, we get the bulk cohesive energy  $E_B(\infty)$  to be  $1.8 \pm 0.1 \text{ eV}$ . This compares with the reported experimental value for Zn cohesive energy of  $1.35 \text{ eV}$ .<sup>35</sup> Various theoretical methods<sup>36–39</sup> have also been employed which lead to a relatively wide range of calculated values (due to the complexity of the electron correlation effects) from 0.97 to 1.91 eV. Compared with the available Zn cohesive energy data, our experimental value is higher than

the reported experiment value but is in reasonable agreement with the theoretical predictions.

## CONCLUSIONS

The evaporation anisotropy phenomenon was observed for in situ generated unsupported Zn NCs using electron microscopic analysis. This anisotropy effect is the result of crystal-face-dependent surface melting. The variation in surface energy between different crystal planes of Zn leads to surface melting, preferentially taking place at  $\{1\bar{1}00\}$  planes of Zn NCs. The observed shape transformation of free Zn NCs under elevated temperatures is fundamentally different from that observed in a traditional hot-stage TEM heating experiments. This suggests that fast evaporation and rapid quenching could be a feasible technique to produce particles with unique shapes by trapping them in metastable configurations.

Using an in-flight tandem DMA-APM method, we also studied the effect of Zn NC size on the onset temperature of evaporation. The size-dependent evaporation is found to be similar to the melting temperature depression of small nanoparticles and analogous to the Kelvin effect. The cohesive energy of bulk Zn is determined to be  $1.8 \pm 0.1 \text{ eV}$  from the size-dependent evaporation data.

## AUTHOR INFORMATION

### Corresponding Author

\*E-mail: mrz@umd.edu.

## ACKNOWLEDGMENT

Financial support for this work comes from an NSF-NIRT grant and the University of Minnesota Initiative for Renewable Energy and the Environment funding project Thermochemical Fuels: Solar at Night. In addition, we wish to acknowledge the microscopy support through the University of Maryland Nanocenter and the University of Maryland NSF-MRSEC.

## REFERENCES

- (1) Goldstein, A. N.; Echer, C. M.; Alivisatos, A. P. Melting in semiconductor nanocrystals. *Science* **1992**, *256* (5062), 1425–1427.
- (2) Lai, S. L.; Guo, J. Y.; Petrova, V.; Ramanath, G.; Allen, L. H. Size-dependent melting properties of small tin particles: Nanocalorimetric measurements. *Phys. Rev. Lett.* **1996**, *77* (1), 99–102.
- (3) Schmidt, M.; Kusche, R.; von Issendorff, B.; Haberland, H. Irregular variations in the melting point of size-selected atomic clusters. *Nature* **1998**, *393* (6682), 238–240.
- (4) Nanda, K. K.; Kruijs, F. E.; Fissan, H. Evaporation of free PbS nanoparticles: Evidence of the Kelvin effect. *Phys. Rev. Lett.* **2002**, *89* (25), 256103.
- (5) Nanda, K. K.; Maisels, A.; Kruijs, F. E.; Fissan, H.; Stappert, S. Higher surface energy of free nanoparticles. *Phys. Rev. Lett.* **2003**, *91* (10), 106102.
- (6) Ajayan, P. M.; Marks, L. D. Experimental-evidence for quasi-melting in small particles. *Phys. Rev. Lett.* **1989**, *63* (3), 279–282.
- (7) Wang, Z. L.; Petroski, J. M.; Green, T. C.; El-Sayed, M. A. Shape transformation and surface melting of cubic and tetrahedral platinum nanocrystals. *J. Phys. Chem. B* **1998**, *102* (32), 6145–6151.
- (8) Cleveland, C. L.; Luedtke, W. D.; Landman, U. Melting of gold clusters. *Phys. Rev. B* **1999**, *60* (7), S065–S077.
- (9) Ahmadi, T. S.; Wang, Z. L.; Green, T. C.; Henglein, A.; El-Sayed, M. A. Shape-controlled synthesis of colloidal platinum nanoparticles. *Science* **1996**, *272* (5270), 1924–1926.

- (10) El-Sayed, M. A. Some interesting properties of metals confined in time and nanometer space of different shapes. *Acc. Chem. Res.* **2001**, *34* (4), 257–264.
- (11) Frenken, J. W. M.; Hinch, B. J.; Toennies, J. P.; Woll, C. Anisotropic diffusion at a melting surface studied with He-atom scattering. *Phys. Rev. B* **1990**, *41* (2), 938–947.
- (12) Pluis, B.; Vandergon, A. W. D.; Frenken, J. W. M.; Vanderveen, J. F. Crystal-face dependence of surface melting. *Phys. Rev. Lett.* **1987**, *59* (23), 2678–2681.
- (13) Ma, X.; Zachariah, M. R. Oxidation anisotropy and size-dependent reaction kinetics of zinc nanocrystals. *J. Phys. Chem. C* **2009**, *113* (33), 14644–14650.
- (14) Liu, H. T.; Armitage, A. F.; Woodruff, D. P. Anisotropy of initial oxidation-kinetics of nickel single-crystal surfaces. *Surf. Sci.* **1982**, *114* (2–3), 431–444.
- (15) Munoz-Marquez, M. A.; Tanner, R. E.; Woodruff, D. P. Surface and subsurface oxide formation on Ni(100) and Ni(111). *Surf. Sci.* **2004**, *565* (1), 1–13.
- (16) Madey, T. E.; Chen, W.; Wang, H.; Kaghazchi, P.; Jacob, T. Nanoscale surface chemistry over faceted substrates: Structure, reactivity and nanotemplates. *Chem. Soc. Rev.* **2008**, *37* (10), 2310–2327.
- (17) Steinfeld, A. Solar hydrogen production via a two-step water-splitting thermochemical cycle based on Zn/ZnO redox reactions. *Int. J. Hydrogen Energy* **2002**, *27*, 611–619.
- (18) Zhang, J. M.; Wang, D. D.; Xu, K. W. Calculation of the surface energy of hcp metals by using the modified embedded atom method. *Appl. Surf. Sci.* **2006**, *253* (4), 2018–2024.
- (19) Ma, X.; Zachariah, M. R. Size-resolved kinetics of Zn nanocrystal hydrolysis for hydrogen generation. *Int. J. Hydrogen Energy* **2010**, *35* (6), 2268.
- (20) Liu, B. Y. H.; Pui, D. Y. H. Equilibrium bipolar charge-distribution of aerosols. *J. Colloid Interface Sci.* **1974**, *49* (2), 305–312.
- (21) Liu, B. Y. H. P.; D., Y. H. *J. Colloid Interface Sci.* **1974**, *47*, 155–171.
- (22) Knutson, E. O.; Whitby, K. T. Anomalous unipolar diffusion charging of polystyrene latex aerosols. *J. Colloid Interface Sci.* **1975**, *53* (3), 493–495.
- (23) Ehara, K.; Hagwood, C.; Coakley, K. J. Novel method to classify aerosol particles according to their mass-to-charge ratio—Aerosol particle mass analyser. *J. Aerosol Sci.* **1996**, *27* (2), 217–234.
- (24) Lall, A. A.; Ma, X.; Guha, S.; Mulholland, G. W.; Zachariah, M. R. Online nanoparticle mass measurement by combined aerosol particle mass analyzer and differential mobility analyzer: Comparison of theory and measurements. *Aerosol Sci. Technol.* **2009**, *43* (11), 1075–1083.
- (25) Zhou, L.; Rai, A.; Piekielek, N.; Ma, X. F.; Zachariah, M. R. Ion-mobility spectrometry of nickel nanoparticle oxidation kinetics: Application to energetic materials. *J. Phys. Chem. C* **2008**, *112* (42), 16209–16218.
- (26) Dash, J. G.; Rempel, A. W.; Wettlaufer, J. S. The physics of premelted ice and its geophysical consequences. *Rev. Mod. Phys.* **2006**, *78* (3), 695–741.
- (27) van der Veen, B. P.; Denier van der Gon, A. W. Surface Melting. In *Chemistry and Physics of Solid Surfaces*; Vanselow, R. H., Ed.; Springer: New York, 1988; Vol. VII, pp 455–490.
- (28) Nanda, K. K.; Maisels, A.; Kruis, F. E.; Rellinghaus, B. Anomalous thermal behavior of gold nanostructures. *EPL* **2007**, *80* (5), S6003.
- (29) Law, J. B. K.; Boothroyd, C. B.; Thong, J. T. L. Site-specific growth of ZnO nanowires from patterned Zn via compatible semiconductor processing. *J. Cryst. Growth* **2008**, *310* (10), 2485–2492.
- (30) Gao, P. X.; Lao, C. S.; Ding, Y.; Wang, Z. L. Metal/semiconductor core/shell nanodisks and nanotubes. *Adv. Funct. Mater.* **2006**, *16* (1), 53–62.
- (31) Tajima, N.; Fukushima, N.; Ehara, K.; Sakurai, H. Mass range and optimized operation of the aerosol particle mass analyzer. *Aerosol Sci. Technol.* **2011**, *45* (2), 196–214.
- (32) Nanda, K. K. Bulk cohesive energy and surface tension from the size-dependent evaporation study of nanoparticles. *Appl. Phys. Lett.* **2005**, *87* (2), 02190.
- (33) Wang, T. H.; Zhu, Y. F.; Jiang, Q. Size effect on evaporation temperature of nanocrystals. *Mater. Chem. Phys.* **2008**, *111* (2–3), 293–295.
- (34) Yang, C. C.; Li, S. Size-dependent phase stability of silver nanocrystals. *J. Phys. Chem. C* **2008**, *112* (42), 16400–16404.
- (35) *CRC Handbook of Chemistry and Physics*, 89; CRC Press: Boca Raton, FL, 2008–2009.
- (36) Philipsen, P. H. T.; Baerends, E. J. Cohesive energy of 3d transition metals: Density functional theory atomic and bulk calculations. *Phys. Rev. B* **1996**, *54* (8), S326–S333.
- (37) Wedig, U.; Jansen, M.; Paulus, B.; Rosciszewski, K.; Sony, P. Structural and electronic properties of Mg, Zn, and Cd from Hartree-Fock and density functional calculations including hybrid functionals. *Phys. Rev. B* **2007**, *75* (20), 205123.
- (38) Gaston, N.; Paulus, B. Ab initio correlation calculations for the ground-state properties of group-12 metals Zn and Cd. *Phys. Rev. B* **2007**, *76* (21), 214116.
- (39) Gaston, N.; Paulus, B.; Wedig, U.; Jansen, M. Multiple minima on the energy landscape of elemental zinc: A wave function based ab initio study. *Phys. Rev. Lett.* **2008**, *100* (22), 226404.